Catalysis Science & Technology
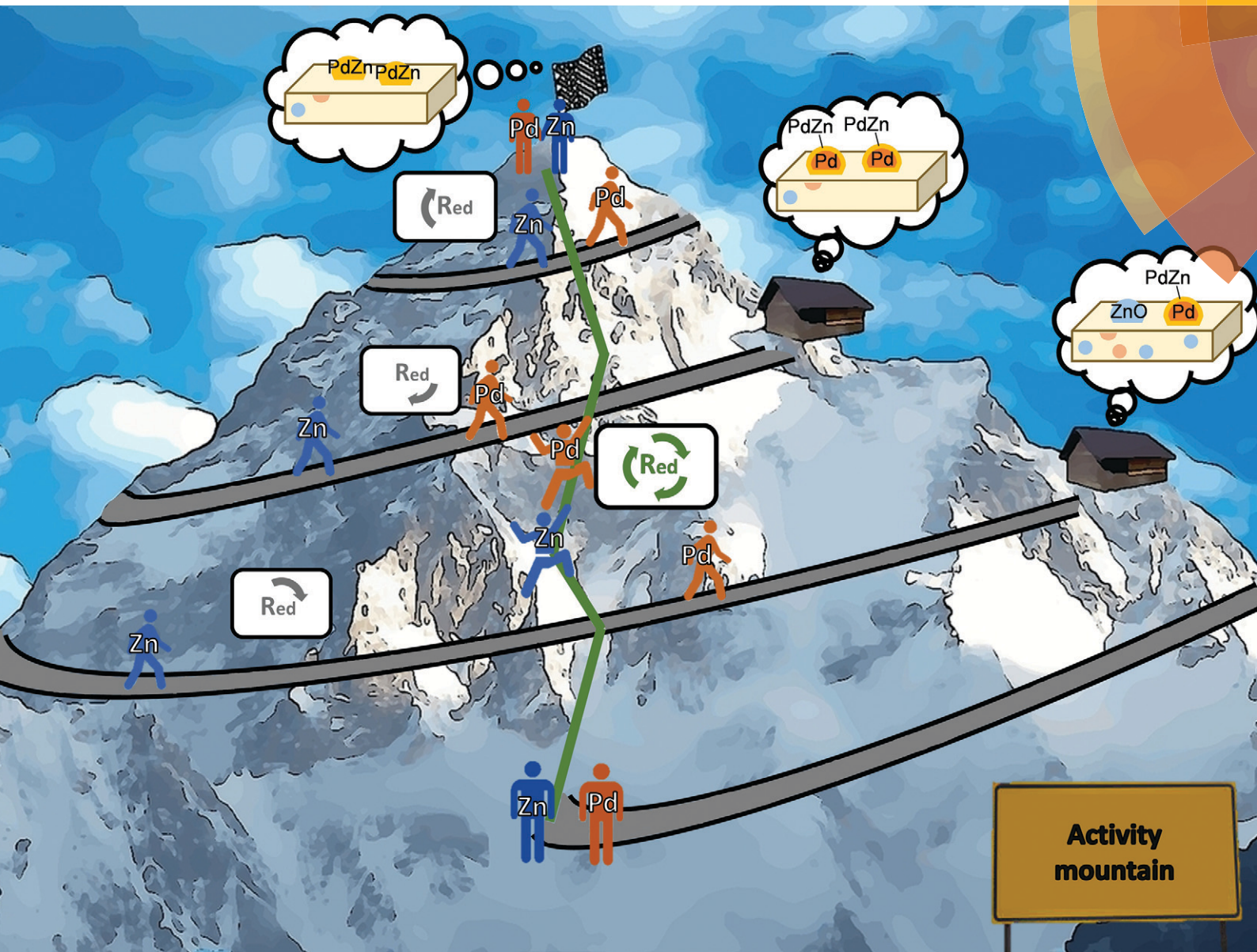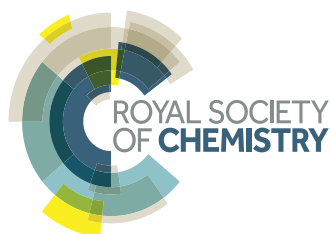
ROYAL SOCIETY
OF CHEMISTRY

PAPER
V. V. Galvita, J. W. Thybaut *et al.*
Formation and stability of an active PdZn nanoparticle catalyst on a
hydrotalcite-based support for ethanol dehydrogenation

PAPER

Check for updates

Formation and stability of an active PdZn nanoparticle catalyst on a hydrotalcite-based support for ethanol dehydrogenation†

J. De Waele, [iD] [a] V. V. Galvita,*[a] H. Poelman, [iD] [a]
C. Detavernier[b] and J. W. Thybaut [iD] *[a]

A hydrotalcite-based PdZn nanoparticle catalyst, PdZn/Mg(Al)(Pd)(Zn)O$_x$ has been synthesized *via* a one-pot procedure. The activation comprising H$_2$ and air treatment(s) allows tuning the nanoparticle formation and, hence, the catalyst performance. Based on an elaborate set of characterization data from EXAFS, *in situ* XRD, STEM and CO chemisorption, it is concluded that single reduction leads to the formation of Pd-rich alloy nanoparticles, *i.e.*, a PdZn shell with a Pd core. Cycled reduction, *i.e.*, 3 subsequent hydrogen and air treatments, ensures the formation of more homogeneously mixed PdZn nanoparticles. Compared with a PdZn/ZnO reference catalyst, the nanoparticles obtained after cycled reduction exhibit a higher initial average turnover frequency in ethanol dehydrogenation, *i.e.*, 7.0 molEtOH (mol$_{Pd}$ s)$^{-1}$ rather than 3.2 molEtOH (mol$_{Pd}$ s)$^{-1}$. An activity loss is observed during the first hours on stream. It is attributed to coking of the Pd sites which are also deemed responsible for acetaldehyde decomposition. Hence, the acetaldehyde selectivity steadily increases during the first hours on stream. Subsequently, the acetaldehyde space time yield and selectivity stabilize at 0.7 × 10^{-4} mol s^{-1} kg$^{-1}_{Pd}$ and 98%, respectively.

1. Introduction

Bimetallic nanoparticles typically exhibit interesting catalytic properties, distinct from those of the respective bulk metals.[1] Quite often higher activities and selectivities are obtained.[2–4] The catalyst particle size may play a determining role in the ultimate performance as a result of a geometric effect. For certain reactions to occur, a well-defined configuration of atoms is required, the number of such active sites depending on the particle size. Furthermore, bimetallic nanoparticles often exhibit electronic effects which differentiate their catalytic properties from those of their monometallic counterparts. Due to alloying of the atoms, a change in the interaction of reactants and products with the electronic levels of the surface sites occurs, as stated by Sabatier.[5–8] Thanks to the tunable ratio of active metals, bimetallic catalyst performance can be optimized.[9–11]

Bimetallic catalysts are extensively studied since they can mimic the catalytic behavior of a monometallic catalyst offering the benefit of an improved stability.[12] An example for this

[a] Laboratory for Chemical Technology, Ghent University, Technologiepark 914, B-9052 Zwijnaarde, Belgium. E-mail: Vladimir.Galvita@UGent.be, Joris.Thybaut@UGent.be
[b] Department of Solid State Sciences, COCOON, Ghent University, Krijgslaan 281/S1, B-9000 Ghent, Belgium
† Electronic supplementary information (ESI) available: Extra XRD, XAS, TEM-EDX, activity testing and XPS results. See DOI: 10.1039/c7cy01105a

are PdZn catalysts as an alternative for Cu in ethanol dehydrogenation to acetaldehyde.

$$CH_3CH_2OH \rightleftharpoons CH_3CHO + H_2$$
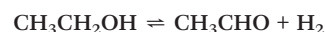
The use of Cu as a catalyst for this reaction and the dehydrogenation of other alcohols has already been intensively investigated and is still being actively explored.[13–24] Cu is also being investigated for the photocatalytic dehydrogenation of ethanol.[25] The major side reaction is the consecutive transformation of acetaldehyde into ethyl acetate. If selective dehydrogenation of ethanol to acetaldehyde can be achieved with high activity, acetaldehyde may become a platform molecule in a bio-based chemical industry, *e.g.*, for the production of 1,3-butadiene, pyridine, ethyl acetate,....[26] Iwasa *et al.* have studied both Pd/ZnO and Cu/ZnO for ethanol dehydrogenation and have observed a higher turnover frequency (TOF) for Pd/ZnO.[27]

The stability of the Cu catalyst in ethanol dehydrogenation is a matter of concern because of metal sintering.[14,15,17,22] Chang *et al.* have obtained a more stable catalyst *via* Cu impregnation on rice husk ash rather than on SiO$_2$, *i.e.*, an activity loss of only 12.5% was observed compared to 20% after 4 h on stream.[17] Tu *et al.* have added Cr as a promoter to prevent Cu sintering.[15] The most stable catalyst was the one with a 4/40 molar ratio of Cr/Cu. However, even then an activity loss amounting to 9% after 8 h time on stream remained.

These authors also proved that the deactivation was due to sintering by correlating the activity with the Cu/Cr surface area. In view of industrial applications, irreversible deactivation should be avoided and, in this respect, PdZn could provide a solution. Intermetallic PdZn catalysts exhibit similar electronic properties as Cu, but the presence of Zn prevents Pd from sintering and, hence, the catalyst retains an activity close to its initial one.[28–30] Also, for methanol steam reforming, a reaction similar to ethanol dehydrogenation, intermetallic PdZn catalysts have been reported to outperform Cu-based ones.[28]

The synthesis of bimetallic nanoparticles typically entails a complicated procedure at the laboratory scale, not to mention the industrial one. Several lab scale techniques such as seeded growth method, atomic layer deposition (ALD),… have recently been reported.[31–36] Wet incipient impregnation and incorporation of the active metals in the support appear to offer promising perspectives for implementation at a larger scale.[2,37,38] Indeed, incorporation of the active metals within the support *via* a one pot synthesis is an easy and reproducible route for bimetallic catalyst synthesis. For propane dehydrogenation into propene, incorporation of the active metals in a hydrotalcite-based support has already proven to yield superior catalysts when compared with wet incipient impregnation.[39] *Via* the incorporation of the active materials in a single-phase hydrotalcite-based precursor, stable nanoparticle catalysts are obtained after calcination and reduction.[37–45]

Hydrotalcite-based catalysts currently gain interest due to promising properties, such as active phase dispersion and stability, both in metal and in base catalysis.[38–51] Their composition is denoted as $[M_{1-x}^{2+}M_x^{3+}(OH)_2]^{x+}\left(A_{x/n}^{n-}\right)\cdot mH_2O$. Mg and Al are commonly used as divalent and trivalent metal ions, but can also be partially replaced, or even completely, by other elements such as transition metals. Hydrotalcites consist of a layered structure where the metals are linked by OH-groups. To compensate for the charge induced by the replacement of a bivalent with a trivalent metal-ion, CO_3^{2-} is present between the layers as well as excess H_2O. Upon calcination, water is released from the lattice, resulting in a collapse of the structure and formation of mixed oxides with a high specific surface area and a small crystal size. After reduction, well-dispersed metallic particles are obtained from the alternative metals incorporated into the mixed oxide $Mg(Al)O_x$ structure. The main advantages of hydrotalcite-based supports for metal catalysis are the uniform distribution of elements by incorporation into the hydrotalcite structure, their moderate basicity which inhibits coking, and their thermal stability towards steam and reduction–oxidation cycling. Furthermore, the presence of Al-cations enhances the resistance to sintering.[38,41–44,51,52]

Deactivation due to coking on metal clusters is often reported as the cause of activity decline of hydrotalcite-based bimetallic catalysts.[41,43,52] Hence, the development of activation or regeneration procedures is of significant importance

for enhancing the catalyst life-time and its potential commercial exploitation. Akporiaye *et al.*[52] investigated the effect of a single reduction as activation procedure for a PtSnCs on hydrotalcite catalyst for propane dehydrogenation, compared to a reduction–oxidation–reduction cycle before the start of the reaction. They observed a higher initial activity and improved stability after such a reduction–oxidation–reduction cycle. Siddiqi *et al.*[43] investigated the fundamental cause for the initial activity loss and increase in selectivity to the desired alkenes during ethane and propane dehydrogenation over Pt. They found that cokes are first formed on the very reactive unalloyed Pt particles and then partially transferred from the Pt particles to the support. This effect is most pronounced for ethane dehydrogenation and results in a less pronounced activity loss due to the migration of cokes to the support. Sun *et al.*[41] support this statement by proving that, for propane dehydrogenation, a small increase in selectivity to propene is observed within the first hour, after which the selectivity becomes stable. This corresponds to a switch from propane conversion into methane and coke on unalloyed Pt particles to conversion into propene on intermetallic PtIn particles.[41] More recently, Redekop *et al.* proved the migration of coke from the Pt particles to the support by means of TAP.[53]

In this work, the one-pot synthesis of an intermetallic PdZn catalyst is pursued. *Via* incorporation of the active metals in a hydrotalcite material, with subsequent calcination and reduction, PdZn nanoparticles are obtained on a mixed oxide. The activity of this catalyst is tested for ethanol dehydrogenation and compared with a benchmark PdZn/ZnO catalyst which has already been described in literature for the same reaction.[27,54–57] The activation procedure is of key importance for the ultimate catalyst performance, more particularly, its stability. Therefore, single reduction, *i.e.*, hydrogen treatment, and cycled reduction, *i.e.*, alternate hydrogen and air treatments, are compared to clarify the impact of the activation procedure on the catalyst performance and stability.

2. Experimental methods

2.1. Catalyst synthesis

The $Mg(Al)(Pd)(Zn)O_x$ hydrotalcite support was synthesized *via* co-precipitation of a 400 ml solution of 0.5 g $Pd(NO_3)_2\cdot2H_2O$, 1.12 g $Zn(NO_3)_2\cdot6H_2O$, 116.4 g $Mg(NO_3)_2\cdot6H_2O$ and 14.77 g $Al(NO_3)_3\cdot9H_2O$ and a 400 ml solution of 2.4 g Na_2CO_3 and 22.6 g NaOH. This corresponds to 1 wt% Pd and 1.2 wt% Zn, *i.e.*, a 1:2 molar Pd/Zn-ratio. The two solutions were added dropwise to 100 ml deionized water functioning as buffer solution under constant stirring at 323 K and kept under these conditions for 30 min. Afterwards, the solution was aged at room temperature for 20 h. The solution was washed 4 times to remove all free NO_3^-- and CO_3^{2-}-ions and dried at 393 K overnight. The support was then crushed and calcined with a ramp of 2.5 K min^{-1} to 873 K and kept at this temperature for 2 h.

PdZn/ZnO was prepared as a reference catalyst. ZnO was first synthesized *via* addition of NH_4OH to $Zn(NO_3)_2 \cdot 6H_2O$ dissolved in H_2O. Thereby ZnO is precipitated and subsequently filtered off and dried. It is then calcined with the same procedure as mentioned before for the $Mg(Al)(Pd)(Zn)O_x$ catalyst. Subsequently, 1 wt% Pd is added to ZnO *via* wet incipient impregnation *via* the addition of a solution of $Pd(NO_3)_2 \cdot 2H_2O$ in ethanol to the ZnO support under constant stirring. Afterwards, the catalyst is again dried and calcined *via* the procedures as mentioned above.

2.2. Catalyst characterization

The bulk chemical composition of the calcined and spent catalyst was determined by means of inductively coupled plasma optical emission spectrometry (ICP-OES) (ICAP 6500 system, Thermo Scientific). The samples were mineralized by fusion with sodium peroxide and dissolution in a mixture of HNO_3, HF and $HClO_4$.

The Brunauer–Emmett–Teller (BET) surface area of the catalyst was determined *via* N_2 adsorption at 77 K in a Gemini V Micromeritics set-up. The samples were first degassed for 12 h at 473 K to remove any volatile adsorbates from the surface.

X-ray photoelectron spectroscopy (XPS) was performed using an S-Probe Monochromatized XPS spectrometer from Surface Science Instruments (VG) with a monochromatic 1486.6 eV AlKα X-ray source. The spectra were recorded with a source power of 200 W. The samples were tilted 45° relative to the analyzer. The base pressure at measurement was 5×10^{-7} Pa. Detailed windows of C1s, Al2s, Mg2s, Pd3d, Zn2p and O1s were recorded with a pass energy of 107.8 eV and a step of 0.1 eV. Energy calibration was performed by alignment of the C1s signal to 284.6 eV.

In situ XRD was performed on the calcined sample, while conducting redox cycles, and on spent samples during an O_2-TPO treatment. A full scan was measured prior to and after each *in situ* measurement. These measurements have been acquired in a Bruker-AXS D8 Discover which emits Cu Kα radiation with a wavelength of 0.154 nm. For the *in situ* measurements, an in-house built reaction chamber with a Kapton foil for X-ray transmission was used. A linear detector covers an angular range of 20° with a resolution of 0.1° and an acquisition time of 10 s. 10 mg of sample was evenly spread on a Si wafer. No interaction between the sample and the wafer was observed. Prior to the analysis, the chamber was evacuated to 4 Pa and flushed. For the redox cycles, a temperature ramp of 50 K min^{-1} was applied to 823 K at which the cycles were performed. Reduction was performed with 10% H_2/He and oxidation with pure oxygen. The O_2-TPO was performed with a temperature ramp of 10 K min^{-1} to 873 K.

In order to investigate the alloy formation, XAS experiments were performed at the DUBBLE beamline of the 6 GeV European Synchrotron Radiation Facility (ESRF) in Grenoble (France) in 16 bunch mode. Both the Pd K-edge, at 24 365 eV, and the Zn K-edge, at 9673 eV, were measured in transmis-

sion mode. For both edges, pellets where prepared with a mass of about 150 mg. No dilution was used. The optics alignment and energy referencing were performed using a Pd and Zn foil, respectively. The XANES scans took ±2 minutes, while EXAFS scans were recorded in ±6 minutes. Gas flows were delivered *via* the DUBBLE gas rig system.[58] An in-house built Microtomo Furnace was used with a Ni sample holder and a clamp hole of 3 mm. It was heated by a Thermocoax 40 W Temp. An EXAFS scan of the as prepared sample was taken under a He flow of 1.23 mol s^{-1}. The calcination was performed in 0.53 mol s^{-1} 20 wt% O_2/He with a temperature ramp of 20 K min^{-1} to 873 K. The sample was then cooled in 20 wt% O_2/He and an EXAFS scan was measured. Subsequent reduction was performed in 1.23 mol s^{-1} 5 wt% H_2/N_2 also with a temperature ramp of 20 K min^{-1} to 823 K. After cooling in 5 wt% H_2/N_2, an EXAFS measurement was performed. To finalize the program, the sample was heated to 823 K and 2 oxidation–reduction cycles were performed. Oxidation with 0.53 mol s^{-1} 20 wt% O_2/He and reduction with 1.23 mol s^{-1} 5 wt% H_2/N_2 took 5 minutes each per cycle with 2.5 minutes intermediate flushing with 1.23 mol s^{-1} He. In total the procedure thus took 25 minutes. Experiments were repeated at both edges. XAS data processing was performed with Athena of the Demeter 0.9.24 software package.[59]

Dark field (DF) scanning transmission electron microscopy (STEM) were used for structural analysis. Energy dispersive X-ray spectrometry (EDX) was used for local chemical analysis. These techniques were implemented using a JEOL JEM-2200FS, Cs-corrected microscope operated at 200 kV, which was equipped with a Schottky-type field-emission gun (FEG) and EDX JEOL JED-2300D. All samples were deposited by immersion onto a lacey carbon film on a copper support grid. More than 300 PdZn particles were measured *via* JEOL Simple Measure®. A Gaussian curve was fitted to the data to determine the mean and standard deviation.

To determine the number of active sites, CO chemisorption was performed in an Autochem II 2920 of Micromeritics equipped with a TCD detector and an OmniStar Pfeiffer mass spectrometer. The measurement was performed on PdZn/ZnO and PdZn/Mg(Al)(Pd)(Zn)O$_x$ in a quartz tube with an internal diameter of 10 mm. Prior to CO chemisorption, *in situ* reduction and oxidation of the sample was performed at 823 K with resp. 5 vol% H_2 in He atmosphere and 100% O_2. At a temperature of 200 K, achieved *via* immersion of the tube in isopropanol ice, 1 wt% CO in He atmosphere was pulsed with a pulse loop of 1 ml onto the catalyst. After 10 pulses no significant change was observed in the surface area of the measured peak, hence the surface was saturated with CO.

Temperature programmed oxidation of the spent samples was performed in the same Autochem equipment, at atmospheric pressure in a 10 mol% O_2 in He atmosphere. The sample was heated at a rate of 5 K min^{-1} to 873 K and kept at that temperature for 10 min.

This journal is © The Royal Society of Chemistry 2017

Catal. Sci. Technol., 2017, **7**, 3715–3727 | 3717

2.3. Catalytic activity measurements

The activity measurements were performed in a high-throughput kinetics mechanistic investigation set-up comprising 8 plug flow reactors with an internal diameter of 0.011 m and a length of 0.9 m.[60,61] PdZn/Mg(Al)(Pd)(Zn)O$_x$ activated with single reduction and cycled reduction have been subjected to a long-term stability test, *i.e.*, a time on stream of 90 h. PdZn/ZnO was tested for 30 h as a reference. 2 g of catalyst powder was pelletized into flakes and crushed into particles of 250–600 μm to avoid extensive pressure drop and internal mass transfer limitations during the catalytic activity tests. Non-porous sintered α-Al$_2$O$_3$ was used as inert material. It was placed upfront of the catalyst bed to ensure a homogeneous distribution of the reactant mixture. The catalyst bed was mixed with inert material to avoid heat transfer limitations. The absence of external mass and heat transfer limitations, as well as the establishment of the ideal plug flow regime, was verified *via* adequate correlations.[62] The online product analysis was conducted with an Agilent 3000 microGC equipped with four complementary columns and thermal conductivity detectors. The product composition was calculated *via* response factors as determined from the analysis of a known reference mixture and validated by comparison with the response factors as reported by Dietz.[63] Prior to reaction, an *in situ* activation procedure was applied consisting of a H$_2$ reduction at 823 K for 30 min using a flow rate of 5.7×10^{-4} mol s^{-1}, further denoted as 'single reduction', or by alternating a pure H$_2$ and air flow rate of 5.7×10^{-4} mol s^{-1}, *i.e.*, H$_2$–air–H$_2$–air–H$_2$, further denoted as 'cycled reduction'. In between the H$_2$ and air flows, the reactor was flushed with N$_2$ to avoid the simultaneous presence of H$_2$ and O$_2$ in the reactor. The reaction was carried out at a temperature of 533 K, an ethanol partial pressure of 23 kPa and a space time of 36 kg$_{cat}$ s mol^{-1}. The total pressure in the reactor was 0.5 MPa. Ethanol was fed as a liquid and mixed with N$_2$ in a molar N$_2$/ethanol-ratio of 20 before entering the reactor. As such, the reactant mixture was instantaneously vaporized and down-stream condensation in the reactor and analysis section was avoided. Catalyst regeneration was performed *via* oxidation with air and subsequent reduction with H$_2$ at 823 K with a flow rate amounting to 5.7×10^{-4} mol s^{-1} for the singly reduced sample and by alternating H$_2$ and air with a flow rate of 5.7×10^{-4} mol s^{-1} for the cycled reduced sample, *i.e.*, the same procedure as for the activation. The carbon balance was measured for all experiments and was within 5%. The average turnover frequency is defined as the ratio of the molar flow rate of converted ethanol $F_{EtOH}^0 - F_{EtOH}$ to the number of active sites N_{Pd}

$$\text{TOF} = \frac{F_{EtOH}^0 - F_{EtOH}}{N_{Pd}} \quad \left(\text{mol}_{EtOH}\ \text{mol}_{Pd}^{-1}\ \text{s}^{-1}\right) \quad (1)$$

The space time yield of acetaldehyde, STY$_{AcH}$, is defined as the ratio of the molar outlet flow rate of acetaldehyde and the mass of Pd on the catalyst.

$$\text{STY}_{AcH} = \frac{F_{AcH}}{W_{Pd}} \quad \left(\text{mol}_{EtOH}\ \text{s}^{-1}\ \text{kg}_{Pd}^{-1}\right) \quad (2)$$

Selectivities towards product i, S_i, are determined on a carbon atom basis and, hence, are defined by the ratio of the molar flow rate of i produced, *i.e.*, F_i, corrected for the number of carbon atoms in the compound, a_i, to the reacted molar flow rate of ethanol, *i.e.*, $F_{EtOH}^0 - F_{EtOH}$, also corrected for the number of carbon atoms in ethanol, *i.e.*, 2:

$$S_i = \frac{a_i F_i}{2\left(F_{EtOH}^0 - F_{EtOH}\right)} \quad (-) \quad (3)$$

2.4. Temporal analysis of products measurements

Transient experiments were performed in a TAP-3 reactor set-up originally described by Gleaves.[64] The reactor is kept at a high vacuum of 10^{-5}–10^{-6} Pa, created using a turbomolecular and a diffusion pump. A quartz micro-reactor of 47.5 mm length with an internal diameter of 4 mm is packed as so-called thin zone reactor. In this configuration, 15 mg of catalyst is sandwiched between layers of inert material. The experiments were conducted both on the Mg(Al)(Pd)(Zn)O$_x$ catalyst activated by single reduction and on the one activated by cycled reduction. The ethanol feed was prepared *via* the injection of 850 μl ethanol in a liquid vaporizing chamber filled with He and heated to 423 K. The reactant feeding lines and the pulse valves were heated to 423 K. Single-pulse experiments of ethanol were performed at 533 K. Each pulse train in an experiment contains 210 pulses. The number of moles of ethanol in each injected pulse amounted to 9.3×10^{-8} mol and 2.7×10^{-8} mol for the single and cycled reduction, respectively. Data acquisition was performed *via* an Extrel 150QC quadrupole mass spectrometer. A collection time of 3 s was used to record the entire pulse response.

3. Results

3.1. PdZn nanoparticle characterization

The Pd and Zn loading as measured *via* ICP-OES as well as the resulting molar Pd/Zn-ratio are reported in Table 1. The actual loading of the calcined catalyst corresponds well with the nominal one. The loadings aren't altered considerably upon reduction and reaction. The active metals are, hence, stable against leaching. It is also evident from Table 1 that the catalyst surface area slightly decreases upon reduction. This is attributed to the diffusion of Pd and Zn from the support to the surface thereby blocking the smallest pores.

Pd and Zn were incorporated in the support of this catalyst. However, upon calcination and reduction, bulk depletion or segregation can occur, changing the concentration of available active metals at the surface and, hence, also the relative amounts of Pd and Zn available for reaction. To probe

3718 | *Catal. Sci. Technol.*, 2017, **7**, 3715–3727

This journal is © The Royal Society of Chemistry 2017

Table 1 BET surface area and weight percentages of Pd and Zn on PdZn/Mg(Al)(Pd)(Zn)O$_x$, determined via ICP-OES

Treatment	BET surface area (m^2 g$_{cat}^{-1}$)	Pd-loading (wt%)	Zn-loading (wt%)	Zn/Pd-ratio (mol mol^{-1})
Calcined	29 ± 3.0	1.03	1.42	2.24
Singly reduced, after reaction	23 ± 5.2	0.93	1.26	2.22
Cycled reduced, after reaction	17 ± 2.0	1.12	1.55	2.21

the surface composition, XPS has been performed (see ESI† for the detailed results). The surface concentrations of Pd and Zn are listed in Table 2. Zn and Pd diffuse from the support to the surface upon single reduction, but the presence of Pd at the surface is enhanced by applying cycled reduction. The overall higher values for Zn can be attributed to easier diffusion of Zn from the support compared to Pd.[65] To determine the chemical nature of Pd and Zn, the position of the peaks relative to the reference C1s was determined, see Table 2. It is evident from the values reported in this table that both the singly and cycled reduced catalyst tend towards the chemical nature of metallic Pd and Zn which have a binding energy of resp. 335.5 eV for Pd3d$_{5/2}$ and 1021.5 eV for Zn2p$_{3/2}$ and a kinetic energy of 988 eV for Zn$_{L_3M_{45}M_{45}}$. The discrepancy between the reported values in Table 2 and the values for metallic Pd and Zn suggests the formation of a different state, such as an alloy. Additional characterization techniques will be used further to confirm that an alloy is actually formed.

3.1.1. Effect of redox cycling on the nanoparticle formation. When performing redox cycles at 873 K in *in situ* XRD, the formation and decomposition of the PdZn intermetallic phase can be directly observed, see Fig. 1. Diffraction peaks at 36.94° and 42.92° (PDF 00-045-0946) are characteristic for MgO, *i.e.*, the support. These peaks remain present during oxidation and reduction. Between 33° and 35°, diffraction peaks corresponding to PdO (PDF 00-041-1107) and ZnO (PDF 00-036-1451) are observed during oxidation, see Fig. 1. These disappear when subjecting the sample to hydrogen and a peak attributed to PdZn (PDF 00-006-0620) appears at 41.19°, as indicated with the downward arrow on Fig. 1 and visualized in the intensities of PdO, ZnO and PdZn. An induction period is observed before this PdZn phase appears. Upon oxidation, the changes occur practically instantaneously. The different kinetics stem from the dilution of H$_2$ in He compared to the use of pure O$_2$ for oxidation.

For both reduction and oxidation treatments, the transformation of PdZn to PdO and *vice versa*, occurs *via* an intermediate monometallic Pd state, as can be seen in Fig. 1. PdO is hence fully reduced prior to the intermetallic compound formation. Furthermore, upon oxidation, Zn is extracted and oxidized first from the intermetallic parti-

cle before Pd oxidation occurs. It can be noted that the peaks corresponding with PdO and ZnO disappear completely upon reduction, indicating that all active material is transformed into PdZn particles.

3.1.2. Oxidation state determination. To further validate the XRD results and investigate the formation of the PdZn intermetallic phase, XAS experiments have been performed. Fig. 2 illustrates the spectra at the Pd K-edge at different stages of catalyst formation: as prepared, calcined, singly reduced and cycled reduced. The spectra of Pd foil, PdZn and PdO have been added for comparison. The 'as prepared' catalyst, see Fig. 2a, exhibits a spectrum that closely resembles the one of PdO. This can be attributed to the incorporation of Pd in the hydrotalcite layers, thus surrounding Pd with oxygen atoms. Less clear on the figure, indicated with an arrow, is a small shoulder in the Pd edge which suggests a good interaction with the support. This feature can be related to an atomic distribution of Pd within the layers. The spectrum of the calcined sample, see Fig. 2b, also corresponds with PdO. After single reduction, see Fig. 2c, the spectrum is clearly distinct from the one of PdO but doesn't resemble that of the Pd foil either. It rather retraces that reported by Tew *et al.* and Ota *et al.* as PdZn.[66,67] Given the distinct difference between the obtained spectrum and that of the Pd foil, it is indicative of the formation of an intermetallic phase in this sample. Upon cycled reduction, no further significant change is observed in the spectrum.

To determine the amount of Pd as PdO, PdZn and as free Pd, the XANES spectra of the calcined, singly reduced and cycled reduced sample were fitted using a linear combination of the reference spectra PdO, Pd foil and PdZn.[68] The fits can be found in the ESI.† Their resulting contributions in the catalysts are reported in Table 3. For the calcined catalyst, Pd is mainly present as PdO. For the singly and cycled reduced sample almost 90% of Pd is present as PdZn, indicating that the formation of the catalyst *via* extraction of Pd and Zn from the support to the surface strongly aids in the alloying of most of the Pd into PdZn intermetallic particles. When looking for differences at the Zn K-edge between single and cycled reduction, little difference can be found in the XANES spectra. Again, a linear combination was

Table 2 Metal surface mol fraction $C_{surf,Pd}$ and $C_{surf,Zn}$ and binding and kinetic energies as determined from XPS, after activation

Activation procedure	$C_{surf,Pd}$ (mol%)	$C_{surf,Zn}$ (mol%)	Binding energy Pd3d$_{5/2}$ (eV)	Binding energy Zn2p$_{3/2}$ (eV)	Kinetic energy Zn L$_3$M$_{45}$M$_{45}$ (eV)
Singly reduced	0.94 ± 0.31	3.16 ± 0.31	336.73	1021.38	989.7
Cycled reduced	1.61 ± 0.27	2.21 ± 0.45	336.76	1021.32	989.9

This journal is © The Royal Society of Chemistry 2017

Catal. Sci. Technol., 2017, **7**, 3715–3727 | 3719
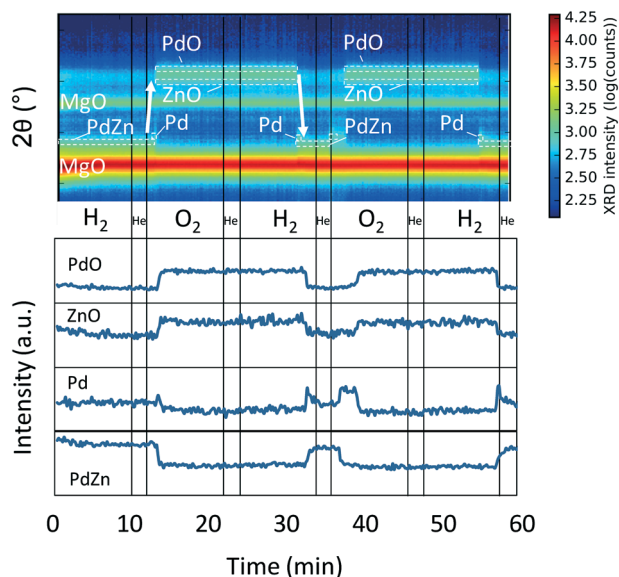
Fig. 1 *In situ* XRD during redox cycles at 873 K. 2D XRD map on top and intensities of PdO, *i.e.*, 34.01°, ZnO, *i.e.*, 35.16°, Pd, *i.e.*, 40.09° and PdZn, *i.e.*, 41.58° at the bottom. The arrows indicate the transformation of PdO and ZnO to PdZn and *vice versa*. The vertical black lines delineate the reduction and oxidation stages.

performed, now using Zn, ZnO, PdZn and ZnAl$_2$O$_4$ as reference spectra (see ESI†).[69,70] The contributions of the reference spectra are also reported in Table 3. Particularly the presence of ZnAl$_2$O$_4$ in the calcined and reduced spectra is remarkable and can be explained from the interaction of Zn with the support. Furthermore, Zn is present as metal upon single reduction, but is included into PdZn after cycled reduction.

3.1.3. Particle size and number of active sites. The particle size was determined by means of STEM. The analysis was performed on a singly reduced sample at 873 K, a cycled reduced one and a sample that was subjected to a second cy-

cled reduction, *i.e.*, 6 reduction–oxidation treatments, see Fig. 3. The catalyst always exhibits a close to unimodal distribution and the average particle size remains constant throughout the treatments, with 5.0 ± 2.5 nm for the singly reduced sample, 5.3 ± 1.8 nm after cycled reduction and 4 ± 2.3 nm after a second cycled reduction. The size of the nanoparticles formed is determined by the synthesis method, *i.e.*, the incorporation of Pd and Zn in the support entails their uniform dispersion in the support such that the metal atoms can remain finely distributed after diffusion towards the surface. This results in a homogeneously mixed distribution of the metal atoms over the hydrotalcite and, hence, in the correspondingly obtained nanoparticles. The particle size of both the singly and cycled reduced sample was found not to change after reaction for the investigated catalyst (see Table S1†).

Since different amounts of active metals diffuse from the support to the surface depending on the reduction procedure, see Table 2, the particle size of the PdZn particles doesn't correlate directly with the number of active sites. Therefore, the number of active sites was determined *via* CO chemisorption. PdZn sites are not active for H$_2$ chemisorption due to the dissociative nature of H$_2$ on Pd and the absence of two adjacent Pd atoms.[71–73] CO pulse chemisorption was performed at 200 K since at room temperature, CO desorbs instantaneously.[73] To eliminate the adsorption of CO on the support, CO chemisorption was also performed on Mg(Al)O$_x$, but none was observed. It can be seen that the number of active sites increases after cycled reduction compared to single reduction. This is in agreement with the observation from XPS that more Pd and Zn atoms have diffused to the surface after cycled reduction, resulting in a higher number of nanoparticles and, hence, more active sites. The number of active sites was also determined for a PdZn/ZnO reference catalyst in view of comparison.
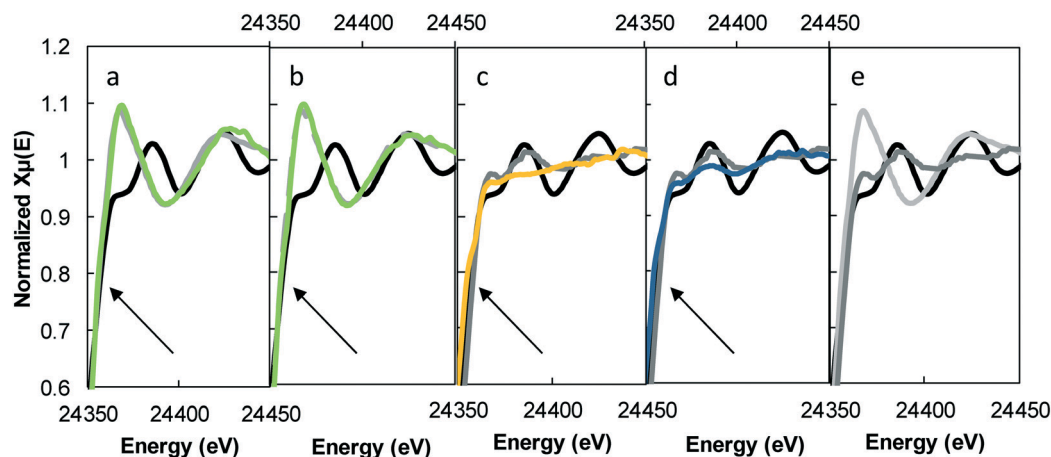

Fig. 2 Comparison of the XANES spectra for PdZn/Mg(Al)(Pd)(Zn)O$_x$ at the Pd K-edge with PdO (light grey), PdZn (dark grey) and Pd foil (black) as reference. The arrow points to a small shoulder in the spectra indicating a good interaction with the support. a: As prepared (green), b: after calcination at 873 K (green), c: after single reduction at 823 K (orange), d: after cycled reduction at 823 K (blue), e: reference spectra: PdO (light grey), PdZn (dark grey) and Pd foil (black).

Table 3 Chemical nature of Pd and Zn determined by least square regression of reference spectra

Activation procedure	Pd as PdZn (%)	Pd as PdO (%)	Pd as Pd (%)	Zn as PdZn (%)	Zn as $ZnAl_2O_4$ (%)	Zn as ZnO (%)	Zn as Zn (%)
Calcined	0	100	0	0	61.06	38.94	0
Singly reduced	88.73	11.27	0	26.07	40.22	22.04	11.67
Cycled reduced	87.81	9.43	2.76	39.26	46.23	14.51	0
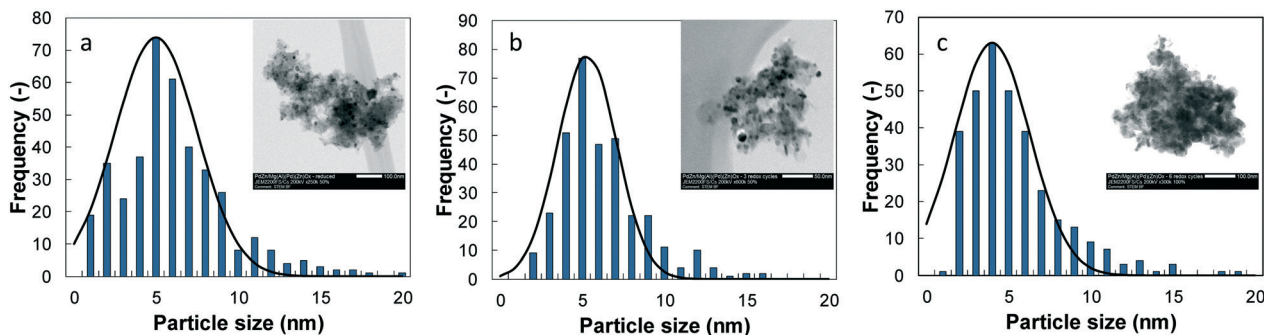
Fig. 3 STEM images of the singly reduced catalyst (a), cycled reduced catalyst (b) and two times cycled reduced catalyst (c).

3.2. Activated catalyst performance

The initial average turnover frequency and acetaldehyde selectivity exhibited by the PdZn/Mg(Al)(Pd)(Zn)O_x catalyst activated *via* single or cycled reduction and the PdZn/ZnO reference catalyst are reported in Table 4. It can be seen that the initial TOF obtained on the singly reduced PdZn/Mg(Al)(Pd)(Zn)O_x is lower than the one on the PdZn/ZnO reference catalyst, but the TOF after cycled reduction is more than the double of that exhibited by the reference catalyst. The acetaldehyde selectivity obtained when using the PdZn/Mg(Al)(Pd)(Zn)O_x catalyst, *i.e.*, 98% after 3 h, is slightly higher than that of the PdZn/ZnO reference catalyst. Other reaction products were methane and carbon monoxide, with selectivities always below 1%.

The evolution of the activity with time on stream of the catalyst activated *via* single or cycled reduction, has been assessed for freshly activated as well as regenerated samples. To represent the activity of the catalyst as a function of time on stream, see Fig. 4, the acetaldehyde space time yield (STY$_{AcH}$) has been used, rather than the turnover frequency. Indeed, a change in TOF is never unambiguous as it can originate from an actual change in activity of each site, or from a change in the number of active sites. The space time yield decreases within the first hours on stream and subsequently stabilizes at resp. 0.15×10^{-4} mol (s kg$_{Pd}$)$^{-1}$ and 0.7×10^{-4}

mol (s kg$_{Pd}$)$^{-1}$ for the singly and cycled reduced samples. As mentioned above, see section 0 and 3.1.3, neither leaching, sintering nor pore collapse could be invoked to explain this decrease in activity, leaving coke formation as the most likely reason for this behavior. Temperature programmed oxidation of the spent samples has been performed to verify this possibility. *In situ* XRD was also performed, but it was impossible to distinguish between cokes and the intermetallic compound PdZn, see ESI.† From the TPO measurements, a broad CO_2-peak was observed at temperatures between 450 K and 700 K, indicating that, indeed, coke had been formed. The amount of coke burnt from the surface was resp. $9.85 \times 10^{-3} \pm 6.95 \times 10^{-3}$ and $6.19 \times 10^{-4} \pm 3.8 \times 10^{-5}$ for the singly and cycled reduced catalyst.

To identify the origin of coke formation, a transient technique, *i.e.*, temporal analysis of products (TAP), was used. This technique aids in investigating the initial stages of the reaction. Single pulse experiments were performed on the samples activated by single and cycled reduction. The integrated yield of hydrogen, methane, carbon monoxide and acetaldehyde has been plotted in Fig. 5 against the number of pulses. In the first pulses, the response of hydrogen amounts to resp. 0.15×10^{-6} mol and 0.5×10^{-6} mol for the singly and cycled reduced catalyst, but decreases significantly during the first 50 pulses. The acetaldehyde production by the cycled

Table 4 Number of active sites determined by means of CO pulse chemisorption, and TOF and acetaldehyde selectivity at time on stream 0 h and 3 h

Catalyst	Activation procedure	Number of active sites (mol kg$_{cat}$$^{-1}$)	TOF (TOS = 0 h) (mol$_{EtOH}$ (mol$_{Pd}$ s)$^{-1}$)	Acetaldehyde selectivity (%)	
				TOS = 0 h	TOS = 3 h
PdZn/ZnO		0.88×10^{-3}	3.2	95	96
PdZn/Mg(Al)(Pd)(Zn)O_x	Singly reduced	1.19×10^{-3}	2.2	89	98
	Cycled reduced	1.80×10^{-3}	7.0	93	98

This journal is © The Royal Society of Chemistry 2017

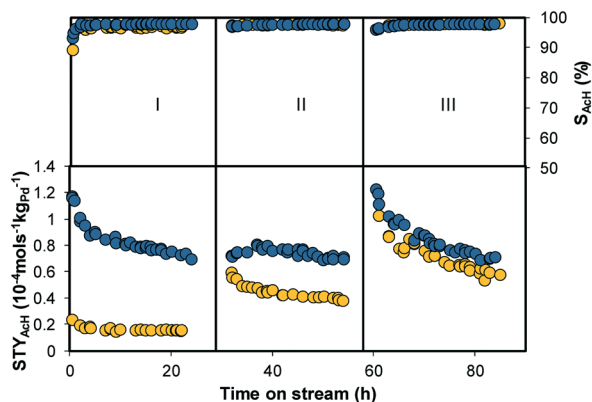*Catal. Sci. Technol.*, 2017, **7**, 3715–3727 | **3721**

Fig. 4 Performance curves of PdZn/Mg(Al)(Pd)(Zn)O$_x$ activated with single reduction (orange) and cycled reduction (blue). I: Freshly activated catalyst, II: catalyst after 1 regeneration, III: catalyst after 2 regenerations.

reduced sample is higher than that of the singly reduced sample, i.e., 1.5×10^{-8} mol for the cycled reduced compared to 1.2×10^{-8} mol for the singly reduced sample. The differences in acetaldehyde production between singly and cycled reduced samples can be related to the presence of more PdZn intermetallic particles after cycled reduction. The methane and carbon monoxide responses coincide, indicating that both are stoichiometrically formed via the same reaction.

4. Discussion

It is clear that the proposed catalyst PdZn/Mg(Al)(Pd)(Zn)O$_x$ activated via cycled reduction exhibits a more interesting ethanol dehydrogenation performance than the PdZn/ZnO reference catalyst, both in terms of activity and acetaldehyde se-
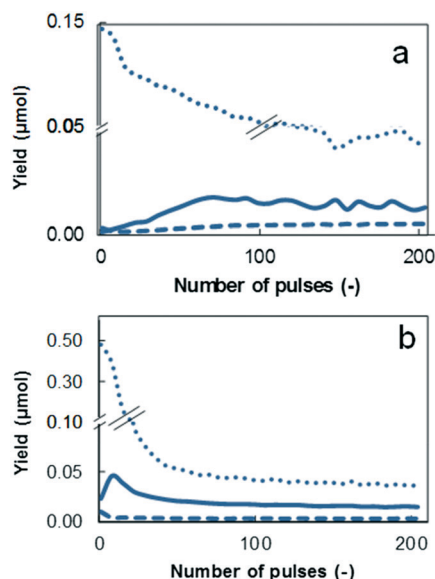

Fig. 5 Evolution of the hydrogen (dotted line), acetaldehyde (full line) and methane and carbon monoxide (coinciding, dashed line) production as a function of pulse number at 533 K for PdZn/Mg(Al)(Pd)(Zn)O$_x$ after single reduction (a) and cycled reduction (b) in TAP.

lectivity, see Table 4. In what follows, three questions are addressed in more detail: which phenomenon is at the origin of the high acetaldehyde selectivity on the PdZn nanoparticles? What renders the PdZn nanoparticle catalyst obtained after cycled reduction so active, compared to the singly reduced one? Which phenomena cause the initial activity loss and simultaneous increase of acetaldehyde selectivity?

4.1. Acetaldehyde selectivity

Only acetaldehyde, methane and carbon monoxide are observed as reaction products. Mavrikakis et al. reported that acetaldehyde decomposition requires two adjacent Pd sites.[27,74] Li et al. have indeed found that the removal of the first H atom from ethanol proceeds on a single site and that this atom subsequently moves to another Pd site.[75] The migration of H to this other Pd site doesn't require the concerned Pd sites to be adjacent whereas this is imperative for acetaldehyde decomposition.[76] The low selectivity to methane and carbon monoxide thus suggests that practically no adjacent Pd sites are present on the investigated catalysts. The characterization discussed in the previous sections allows constructing a schematic representation of the nanoparticle catalysts obtained after single and cycled reduction, see Fig. 6.

Fig. 6 frame a, starts from the calcined material. Pd and Zn are atomically dispersed in the support and some small ZnO clusters are already present on the surface, as confirmed by STEM, see the ESI.† Pd and Zn are present in oxide form, i.e., PdO for Pd and ZnO or ZnAl$_2$O$_4$ for Zn, see Table 3.

Upon H$_2$ treatment at 823 K, Pd and Zn diffuse from the support towards the surface, Pd being more easily reduced, Fig. 6, frame b. It results in the presence of ZnO on the surface, since the reduction temperature of ZnO exceeds 873 K, together with metallic Pd. Later in the hydrogen treatment, excess hydrogen spills over from the Pd particles to ZnO, aiding its reduction to Zn, see Fig. 6, frame c. ZnO can only be reduced in the presence of another metal, such as Cu and Pd, which is able to form an alloy with Zn. ZnO itself only becomes active for H$_2$ adsorption at temperatures exceeding 873 K.[77,78] Thus, spillover of hydrogen from Pd is necessary for the reduction of ZnO (ref. 79) and the subsequent formation of the PdZn intermetallic compound. Zn diffuses into the Pd particle as the employed reduction temperature exceeds its migration temperature, i.e., 823 K vs. 583 K. However, some Zn remains, together with unreduced ZnO, present on the surface of the support, being reduced but unable to diffuse into the Pd particle at that time. It results in Pd-rich alloy nanoparticles, i.e., a Pd core with PdZn shell, see Fig. 6, frame d.[56,80] The XANES fitting after single reduction confirms the Zn excess on the surface, see Table 3.[66,67] Moreover, the presence of Zn in the PdZn layer limits the Pd availability for further H$_2$ activation, since two adjacent Pd sites are required for H$_2$ dissociation. As a result, complete ZnO reduction cannot be achieved after a single reduction.[56] This is

3722 | Catal. Sci. Technol., 2017, 7, 3715–3727

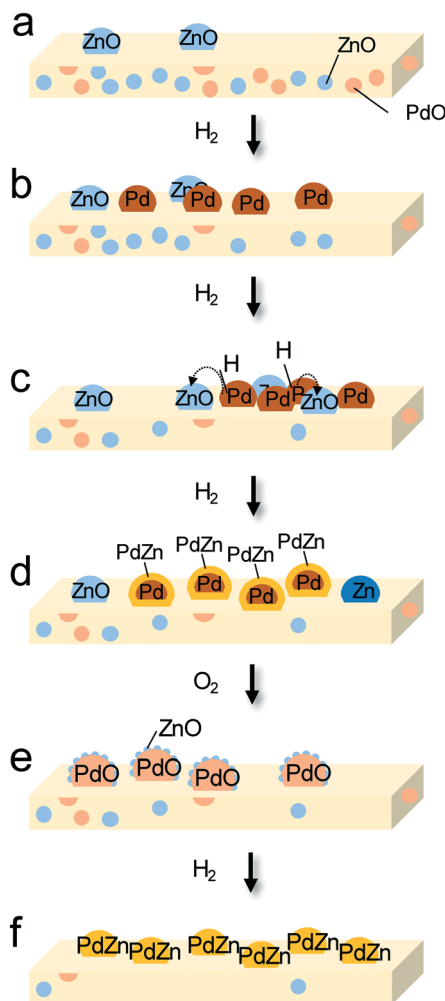This journal is © The Royal Society of Chemistry 2017

Fig. 6 Representation of the formation of the intermetallic compound during single reduction (a–d) and cycled reduction (d–f) at 823 K for PdZn/Mg(Al)(Pd)(Zn)O$_x$. Dark orange: Pd, light blue: ZnO or ZnAl$_2$O$_4$, light orange: PdO, gold: intermetallic compound PdZn.

also reported by Araña *et al.*, who demonstrated that H$_2$ chemisorption experiments did not exhibit any adsorption on PdZn.[72] Tamtögl *et al.* generated additional proof for this more difficult H$_2$ activation by Zn by comparing pure Pd with PdZn *via* TPD.[73] Alloying Pd with Zn does not cause any energetic differences, but the number of adsorption sites decreases. Similar phenomena were also observed by Föttinger *et al.* and Ota *et al.* for PdZn and by Filez *et al.* for PtGa.[56,66,81]

Subjecting the reduced material to oxidation, the intermetallic phase decomposes into PdO and ZnO, according to *in situ* XRD (Fig. 1), see Fig. 6, frame e. *In situ* XRD shows that Zn is first removed from the PdZn particle and subsequently undergoes oxidation, while the particle remains as metallic Pd. Afterwards, also Pd is oxidized to PdO. A second reduction re-establishes the PdZn particles with Zn now being more homogeneously distributed throughout the particle, thereby obtaining homogeneously mixed PdZn particles, as confirmed by XAS, see Table 3 and Fig. 6 frame f. When com-

paring the surface concentrations of both catalysts after single and cycled reduction, see Table 2, it can be seen that the concentration of Pd increases, indicating that subsequent oxidation reduction treatments allow extracting additional Pd from the support. The particle size remains the same irrespective of the number of cycles, see Fig. 3, but the number of active sites increases. Thus, the decomposition and re-establishment of the intermetallic compound leaves the clusters intact indicating a good stability of the particles on the support.

For the reference catalyst PdZn/ZnO, Bahruji *et al.* and Föttinger *et al.* have already investigated the appearance of the catalyst.[54–56] They concluded that PdZn nanoparticles are formed, but overall, larger particles, *i.e.*, in the range of 10–20 nm, are reported for PdZn/ZnO than for the PdZn/Mg(Al)(Pd)(Zn)O$_x$ catalyst discussed in our work. This causes an incomplete diffusion of Zn into the Pd particle, leading to a PdZn shell over a Pd core.

Concluding, both single and cycled reduction give rise to PdZn nanoparticles. These particles are composed of Pd atoms which are surrounded by Zn atoms, as reported by Neyman *et al.*[76] This explains the high acetaldehyde selectivity. Initially, the singly reduced sample gave a lower selectivity due to the Pd-rich nature of the active sites. After 3 h, however, the selectivity remains the same for both activation procedures, since the adjacent Pd sites have been blocked by coke, see also section 4.3. The acetaldehyde selectivity slightly exceeds that from the reference PdZn/ZnO catalyst after 3 h. This could indicate a better homogeneity of the PdZn particles, hence the presence of less adjacent Pd sites, obtained by incorporation.

4.2. Activity

In contrast with the selectivity, the activity of the catalyst does depend on the activation procedure. Overall, the catalyst initial average turnover frequency is high, *i.e.*, 2.2 mol$_{EtOH}$ (mol$_{Pd}$ s)$^{-1}$ for singly reduced and 7.0 mol$_{EtOH}$ (mol$_{Pd}$ s)$^{-1}$ for the cycled reduced catalyst, see Table 4. This is related to the presence of active nanoparticles on the catalysts. The difference in initial average turnover frequency can be explained with the catalyst formation scheme, Fig. 6. Upon reduction by excess H$_2$ spilled over from Pd, Zn diffuses towards and into these Pd metal particles. By doing so, it decreases the number of Pd accessible for H$_2$ molecules and, hence, further ZnO reduction is hindered. This results in Pd-rich alloy nanoparticles with an outer PdZn layer and a Pd core. As described above, only upon cycled reduction, PdZn nanoparticles with a homogeneously mixed composition are formed. Towards the first experimental point, at 0.5 h, rapid coking is taking place, leading to lower activity of the catalyst. This explains also why the singly reduced sample is initially less active than the reference catalyst. For the PdZn/ZnO catalyst, the abundant availability of Zn may result in Pd sites being covered by Zn, thereby reducing the coking, but does not

This journal is © The Royal Society of Chemistry 2017

Catal. Sci. Technol., 2017, 7, 3715–3727 | 3723

induce the homogeneity that is exhibited by the cycled reduced catalyst.[54–56]

Furthermore, it should be taken into account that initially, the acetaldehyde selectivity is slightly lower for the singly reduced sample. This indicates a higher occurrence of two adjacent Pd atoms since more methane and carbon monoxide is produced. The transition state for acetaldehyde decomposition requires the occupancy of two sites whereas ethanol dehydrogenation proceeds on one site and the removed H-atom moves toward a free Pd site in the neighborhood, but not necessarily adjacent.[74–76] Since TOF is defined as number of molecules reacting per site per second, the requirement of two sites biases the calculation of the TOF.

Catalyst regeneration has subsequently been assessed, see Fig. 4, frame II and III. For the singly reduced sample, an oxidation treatment is performed to burn off the coke and consecutive reduction restores the intermetallic nanoparticles. For the cycled reduced catalyst, again a cycled regeneration is performed after the coke burn off. The cycled reduced catalyst maintains its original activity, see the blue circles in Fig. 4, frame II. It can, hence, be concluded that this catalyst is restored after stabilization to the same active state as the freshly activated catalyst. The singly reduced sample exhibits an enhanced performance after regeneration, see Fig. 4, frame II. The additional redox cycle to which the catalyst has been exposed in the regeneration procedure resulted in the extraction of more Pd and Zn from the support, thereby increasing the number of active sites and improving the homogeneity of the PdZn particle. This explains why, after two regenerations, *i.e.*, subsequent air and hydrogen treatment, the average turnover frequency of acetaldehyde is comparable for the singly and the cycled reduced sample. After regeneration, the singly reduced catalyst, in fact, behaves like the cycled reduced catalyst. When taking into account the chemical nature of Pd and Zn present on the surface before and after reaction, see the ESI,† it can be seen that Pd and Zn both evolve towards the metallic state. It can, hence, be assumed that all Pd and Zn have indeed been extracted from the support and homogeneously distributed throughout the particle.

It can be concluded that performing a cycled reduction is beneficial for the catalyst performance and stability. A single reduction treatment doesn't suffice to convert all ZnO to Zn and let it diffuse into Pd. Furthermore, synthesis of the catalyst *via* incorporation of the active metals and cycled reduction gives rise to a more active catalyst compared to the PdZn/ZnO reference catalyst. Furthermore, regeneration with the same cycled reduction restores the initial activity, indicating that the catalyst composition is not altered upon regeneration.

4.3. Initial activity loss

The catalyst experiences an initial activity loss irrespective of the activation procedure. The methane selectivity decreases simultaneously with this activity loss (see Fig. S7†), while that of acetaldehyde increases to close to 100%, see Fig. 4. Based on the results in.

Table 1, it can be concluded that the catalyst's surface area doesn't change significantly, such that an explanation for the activity loss will not be situated in this direction. Also sintering and leaching could be excluded as potential causes for the activity loss, since the particle size and metal loading remain the same after reaction, see Table S1† and Table 1. This represents a considerable improvement compared with commercial Cu catalysts where irreversible deactivation due to sintering has been proven to be a major drawback.[14,15,17,22]

TPO and TAP results indicate that coke formation is at the origin of the activity loss. Based on the reactions represented in Fig. 7, it can be seen that, if only reactions (1) and (2) would occur, the hydrogen production, in Fig. 5, should equal the sum of the acetaldehyde and methane production. A higher hydrogen production than expected from the stoichiometry of those two reactions, hence, indicates the occurrence of an additional reaction such as reaction (3) in Fig. 7. Indeed, when methane decomposes into coke, more hydrogen is produced, explaining the initial pulse responses observed in the TAP measurements. In subsequent pulses, the hydrogen production per pulse decreases, but still exceeds the amount expected based on reactions (1) and (2). During the first pulses, a rapid blockage of adjacent Pd sites occurs by coke *via* reactions (1) to (4). Afterwards, a slower activity loss occurs, possibly related to the migration of cokes towards the support and the recoking of adjacent Pd sites. This coking behavior eventually disappears and leaves the PdZn sites intact, resulting in a stable and selective conversion to acetaldehyde.

When combining all results discussed above, the stable space time yield of the activated samples, *i.e.*, Fig. 4, can be explained. The lower STY of the singly reduced catalyst compared to the cycled reduced, is attributed to a lower amount of active sites and to rapid coking of the adjacent Pd sites. Upon cycled reduction, more active sites are formed with a homogeneously mixed composition of the PdZn particle which reduces the coking. It can be noted that, for both catalysts, coking blocks adjacent neighboring Pd-sites, improving the selectivity towards acetaldehyde. After the initial activity changes, the catalyst, activated by single or cycled reduction, remains stable which opens up perspectives for commercial applications in the production of acetaldehyde.
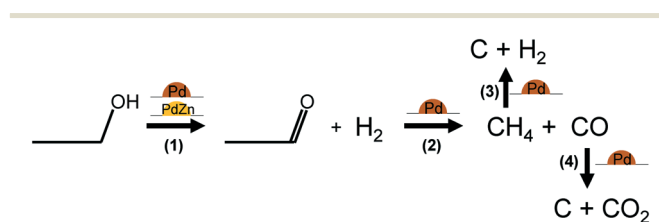

Fig. 7 Schematic representation of the reaction mechanism on a PdZn catalyst. Gold: PdZn particles, orange: Pd-rich particles.

3724 | *Catal. Sci. Technol.*, 2017, **7**, 3715–3727

This journal is © The Royal Society of Chemistry 2017

The best catalyst discussed in this work, *i.e.*, the cycled reduced PdZn/Mg(Al)(Pd)(Zn)O$_x$ catalyst, exhibits an improved selectivity compared to PdZn/ZnO and a stable activity after a few hours, allowing for a long term use of this catalyst in a potential industrial application.

5. Conclusions

PdZn/Mg(Al)(Pd)(Zn)O$_x$, a PdZn nanoparticle catalyst prepared *via* a one-pot synthesis of a hydrotalcite-based support, exhibits promising features as an alternative catalyst to Cu for ethanol dehydrogenation. Its activity can be tuned *via* the adopted activation procedure. After single reduction an initial average TOF of 2.2 mol$_{EtOH}$ (mol$_{Pd}$ s)$^{-1}$ is achieved whereas cycled reduction, *i.e.*, a sequence of hydrogen and air treatments, enhances this initial average TOF to 7.0 mol$_{EtOH}$ (mol$_{Pd}$ s)$^{-1}$. After 3 h, the acetaldehyde selectivity is independent of the activation procedure. Overall, the cycled reduced PdZn/Mg(Al)(Pd)(Zn)O$_x$ catalyst exhibits both a superior activity and selectivity compared to the reference PdZn/ZnO catalyst.

The high acetaldehyde selectivity was achieved *via* the presence of Zn isolating the Pd sites. As a result, acetaldehyde adsorption on two adjacent Pd sites, as necessary for its decomposition into methane and carbon monoxide, is hindered. The main difference between the singly and cycled reduced catalyst is the remaining Pd core after a single reduction. A cycled reduction comprising 3 successive oxidation–reduction treatments is required to entirely convert the Pd core into a mixed PdZn phase.

The initial activity loss and simultaneous, increasing acetaldehyde selectivity are attributed to the coking and, hence, blocking of adjacent Pd sites, *i.e.*, those required for acetaldehyde decomposition. Subsequently, an up to 20 h stable catalyst activity with close to 100% selective acetaldehyde formation on PdZn is observed.

Acknowledgements

References

1 B. C. Gates, in *Preparation of Solid Catalysts*, Wiley-VCH Verlag GmbH, 2008, pp. 371–388, DOI: 10.1002/9783527619528.ch4b.

2 M. Armbrüster, G. Wowsnick, M. Friedrich, M. Heggen and R. Cardoso-Gil, *J. Am. Chem. Soc.*, 2011, **133**, 9112–9118.

3 D. Wang and Y. Li, *Adv. Mater.*, 2011, **23**, 1044–1060.

4 H.-L. Jiang and Q. Xu, *J. Mater. Chem.*, 2011, **21**, 13705–13725.

5 A. K. Singh and Q. Xu, *ChemCatChem*, 2013, **5**, 652–676.

6 N. Toshima and T. Yonezawa, *New J. Chem.*, 1998, **22**, 1179–1201.

7 Z. Wei, J. Sun, Y. Li, A. K. Datye and Y. Wang, *Chem. Soc. Rev.*, 2012, **41**, 7994–8008.

8 B. Coq and F. Figueras, *Coord. Chem. Rev.*, 1998, **178–180**(Part 2), 1753–1783.

9 X. Mao, L. Yang, J. Yang, J. Key, S. Ji, H. Wang and R. Wang, *J. Electrochem. Soc.*, 2013, **160**, H219–H223.

10 W. An, D. Gatewood, B. Dunlap and C. H. Turner, *J. Power Sources*, 2011, **196**, 4724–4728.

11 I. E. L. Stephens, A. S. Bondarenko, F. J. Perez-Alonso, F. Calle-Vallejo, L. Bech, T. P. Johansson, A. K. Jepsen, R. Frydendal, B. P. Knudsen, J. Rossmeisl and I. Chorkendorff, *J. Am. Chem. Soc.*, 2011, **133**, 5485–5491.

12 A. Pang Tsai, S. Kameoka and Y. Ishii, *J. Phys. Soc. Jpn.*, 2004, **73**, 3270–3273.

13 I. C. Freitas, S. Damyanova, D. C. Oliveira, C. M. P. Marques and J. M. C. Bueno, *J. Mol. Catal. A: Chem.*, 2014, **381**, 26–37.

14 N. Kanoun, M. P. Astier and G. M. Pajonk, *Appl. Catal.*, 1991, **70**, 225–236.

15 Y.-J. Tu, C. Li and Y.-W. Chen, *J. Chem. Technol. Biotechnol.*, 1994, **59**, 141–147.

16 K. Inui, T. Kurabayashi and S. Sato, *Appl. Catal., A*, 2002, **237**, 53–61.

17 F.-W. Chang, W.-Y. Kuo and K.-C. Lee, *Appl. Catal., A*, 2003, **246**, 253–264.

18 A. B. Gaspar, F. G. Barbosa, S. Letichevsky and L. G. Appel, *Appl. Catal., A*, 2010, **380**, 113–117.

19 M. Zhang, G. Li, H. Jiang and J. Zhang, *Catal. Lett.*, 2011, **141**, 1104–1110.

20 A. G. Sato, D. P. Volanti, D. M. Meira, S. Damyanova, E. Longo and J. M. C. Bueno, *J. Catal.*, 2013, **307**, 1–17.

21 Q.-N. Wang, L. Shi and A.-H. Lu, *ChemCatChem*, 2015, **7**, 2846–2852.

22 E. Santacesaria, G. Carotenuto, R. Tesser and M. Di Serio, *Chem. Eng. J.*, 2012, **179**, 209–220.

23 Z. Lu, D. Gao, H. Yin, A. Wang and S. Liu, *J. Ind. Eng. Chem.*, 2015, **31**, 301–308.

24 M. Zhang, Y. Huang, R. Li, G. Li and Y. Yu, *Catal. Lett.*, 2014, **144**, 1978–1986.

25 C. Ampelli, R. Passalacqua, C. Genovese, S. Perathoner, G. Centi, T. Montini, V. Gombac, J. J. Delgado Jaen and P. Fornasiero, *RSC Adv.*, 2013, **3**, 21776–21788.

26 J. Sun and Y. Wang, *ACS Catal.*, 2014, **4**, 1078–1090.

27 N. Iwasa, O. Yamamoto, R. Tamura, M. Nishikubo and N. Takezawa, *Catal. Lett.*, 1999, **62**, 179–184.

28 N. Iwasa, T. Mayanagi, W. Nomura, M. Arai and N. Takezawa, *Appl. Catal., A*, 2003, **248**, 153–160.

29 N. Takezawa and N. Iwasa, *Catal. Today*, 1997, **36**, 45–56.

30 K. Föttinger, *Catalysis*, 2013, **25**, 77–117.

31 J. Zhu, M.-L. Yang, Y. Yu, Y.-A. Zhu, Z.-J. Sui, X.-G. Zhou, A. Holmen and D. Chen, *ACS Catal.*, 2015, **5**, 6310–6319.

32 D. Astruc, F. Lu and J. R. Aranzaes, *Angew. Chem., Int. Ed.*, 2005, **44**, 7852–7872.

33 M. A. El-Sayed, *Acc. Chem. Res.*, 2001, **34**, 257–264.

34 H. Bönnemann and Ryan M. Richards, *Eur. J. Inorg. Chem.*, 2001, **2001**, 2455–2480.

35 J. Dendooven, R. K. Ramachandran, K. Devloo-Casier, G. Rampelberg, M. Filez, H. Poelman, G. B. Marin, E. Fonda and C. Detavernier, *J. Phys. Chem. C*, 2013, **117**, 20557–20561.

36 R. K. Ramachandran, J. Dendooven, M. Filez, V. V. Galvita, H. Poelman, E. Solano, M. M. Minjauw, K. Devloo-Casier, E. Fonda, D. Hermida-Merino, W. Bras, G. B. Marin and C. Detavernier, *ACS Nano*, 2016, **10**, 8770–8777.

37 P. P. Sun, G. Siddiqi, M. F. Chi and A. T. Bell, *J. Catal.*, 2010, **274**, 192–199.

38 V. Galvita, G. Siddiqi, P. Sun and A. T. Bell, *J. Catal.*, 2010, **271**, 209–219.

39 M. Filez, E. A. Redekop, H. Poelman, V. V. Galvita, M. Meledina, S. Turner, G. Van Tendeloo, C. Detavernier and G. B. Marin, *Catal. Sci. Technol.*, 2016, **6**, 1863–1869.

40 A. Ota, J. Kröhnert, G. Weinberg, I. Kasatkin, E. L. Kunkes, D. Ferri, F. Girgsdies, N. Hamilton, M. Armbrüster, R. Schlögl and M. Behrens, *ACS Catal.*, 2014, **4**, 2048–2059.

41 P. Sun, G. Siddiqi, W. C. Vining, M. Chi and A. T. Bell, *J. Catal.*, 2011, **282**, 165–174.

42 E. A. Redekop, V. V. Galvita, H. Poelman, V. Bliznuk, C. Detavernier and G. B. Marin, *ACS Catal.*, 2014, **4**, 1812–1824.

43 G. Siddiqi, P. Sun, V. Galvita and A. T. Bell, *J. Catal.*, 2010, **274**, 200–206.

44 K. Takehira, *J. Nat. Gas Chem.*, 2009, **18**, 237–259.

45 P. Li, C. He, J. Cheng, C. Y. Ma, B. J. Dou and Z. P. Hao, *Appl. Catal., B*, 2011, **101**, 570–579.

46 K. K. Rao, M. Gravelle, J. S. Valente and F. Figueras, *J. Catal.*, 1998, **173**, 115–121.

47 T. Baskaran, J. Christopher and A. Sakthivel, *RSC Adv.*, 2015, **5**, 98853–98875.

48 F. Cavani, F. Trifirò and A. Vaccari, *Catal. Today*, 1991, **11**, 173–301.

49 U. Costantino, F. Marmottini, M. Nocchetti and R. Vivani, *Eur. J. Inorg. Chem.*, 1998, **1998**, 1439–1446.

50 D. P. Debecker, E. M. Gaigneaux and G. Busca, *Chem. – Eur. J.*, 2009, **15**, 3920–3935.

51 D. Tichit, M. H. Lhouty, A. Guida, B. H. Chiche, F. Figueras, A. Auroux, D. Bartalini and E. Garrone, *J. Catal.*, 1995, **151**, 50–59.

52 D. Akporiaye, S. F. Jensen, U. Olsbye, F. Rohr, E. Rytter, M. Rønnekleiv and A. I. Spjelkavik, *Ind. Eng. Chem. Res.*, 2001, **40**, 4741–4748.

53 E. A. Redekop, S. Saerens, V. V. Galvita, I. P. González, M. Sabbe, V. Bliznuk, M.-F. Reyniers and G. B. Marin, *J. Catal.*, 2016, **344**, 482–495.

54 H. Bahruji, M. Bowker, G. Hutchings, N. Dimitratos, P. Wells, E. Gibson, W. Jones, C. Brookes, D. Morgan and G. Lalev, *J. Catal.*, 2016, **343**, 133–146.

55 K. Föttinger, *Catal. Today*, 2013, **208**, 106–112.

56 K. Föttinger, J. A. van Bokhoven, M. Nachtegaal and G. N. Rupprechter, *J. Phys. Chem. Lett.*, 2011, **2**, 428–433.

57 A. Karim, T. Conant and A. Datye, *J. Catal.*, 2006, **243**, 420–427.

58 V. Martis, A. M. Beale, D. Detollenaere, D. Banerjee, M. Moroni, F. Gosselin and W. Bras, *J. Synchrotron Radiat.*, 2014, **21**, 462–463.

59 B. Ravel and M. Newville, *J. Synchrotron Radiat.*, 2005, **12**, 537–541.

60 K. Van der Borght, K. Toch, V. Galvita, J. Thybaut and G. Marin, *Catalysts*, 2015, **5**, 1948.

61 N. Navidi, J. W. Thybaut and G. B. Marin, *Appl. Catal., A*, 2014, **469**, 357–366.

62 R. J. Berger, E. H. Stitt, G. B. Marin, F. Kapteijn and J. A. Moulijn, *CATTECH*, 2001, **5**, 36–60.

63 W. Dietz, *J. Chromatogr. Sci.*, 1967, **5**, 68–71.

64 J. T. Gleaves, G. Yablonsky, X. Zheng, R. Fushimi and P. L. Mills, *J. Mol. Catal. A: Chem.*, 2010, **315**, 108–134.

65 J. Pelleg, in *Diffusion in Ceramics*, Springer International Publishing, Cham, 2016, pp. 237–299, DOI: 10.1007/978-3-319-18437-1_13.

66 A. Ota, E. L. Kunkes, I. Kasatkin, E. Groppo, D. Ferri, B. Poceiro, R. M. Navarro Yerga and M. Behrens, *J. Catal.*, 2012, **293**, 27–38.

67 M. W. Tew, H. Emerich and J. A. van Bokhoven, *J. Phys. Chem. C*, 2011, **115**, 8457–8465.

68 A. V. Chistyakov, V. Y. Murzin, M. A. Gubanov and M. V. Tsodikov, *Chem. Eng. Trans.*, 2013, **32**, 619–624.

69 B. G. Ershov, A. V. Anan'ev, E. V. Abkhalimov, D. I. Kochubei, V. V. Kriventsov, L. M. Plyasova, I. Y. Molina, N. Y. Kozitsyna, S. E. Nefedov, M. N. Vargaftik and I. I. Moiseev, *Nanotechnol. Russ.*, 2011, **6**, 323–329.

70 S. Pin, M. Suardelli, F. D'Acapito, G. Spinolo, M. Zema, S. C. Tarantino and P. Ghigna, *J. Phys. Chem. C*, 2013, **117**, 6105–6112.

71 H. Xiong, A. DeLaRiva, Y. Wang and A. K. Datye, *Catal. Sci. Technol.*, 2015, **5**, 254–263.

72 J. Araña, N. Homs, J. Sales, J. L. G. Fierro and P. Ramirez de la Piscina, *Catal. Lett.*, 2001, **72**, 183–189.

73 A. Tamtögl, M. Kratzer, J. Killman and A. Winkler, *J. Chem. Phys.*, 2008, **129**, 224706.

74 M. Mavrikakis and M. A. Barteau, *J. Mol. Catal. A: Chem.*, 1998, **131**, 135–147.

75 M. Li, W. Guo, R. Jiang, L. Zhao and H. Shan, *Langmuir*, 2009, **26**, 1879–1888.

76 K. M. Neyman, K. H. Lim, Z.-X. Chen, L. V. Moskaleva, A. Bayer, A. Reindl, D. Borgmann, R. Denecke, H.-P. Steinruck and N. Rosch, *Phys. Chem. Chem. Phys.*, 2007, **9**, 3470–3482.

77 K.-D. Jung, O.-S. Joo and S.-H. Han, *Catal. Lett.*, 2000, **68**, 49–54.

78 L. Lloyd, *Handbook of Industrial Catalysts*, Springer US, 2011.

79 W. Karim, C. Spreafico, A. Kleibert, J. Gobrecht, J. VandeVondele, Y. Ekinci and J. A. van Bokhoven, *Nature*, 2017, **541**, 68–71.

80 B. Schwab, A. Ruh, J. Manthey and M. Drosik, in *Ullmann's Encyclopedia of Industrial Chemistry*, Wiley-VCH Verlag GmbH & Co. KGaA, 2000, DOI: 10.1002/14356007.a28_509.pub2.

81 M. Filez, E. A. Redekop, V. V. Galvita, H. Poelman, M. Meledina, S. Turner, G. Van Tendeloo, A. T. Bell and G. B. Marin, *Phys. Chem. Chem. Phys.*, 2016, **18**, 3234–3243.

This journal is © The Royal Society of Chemistry 2017

Catal. Sci. Technol., 2017, **7**, 3715–3727 | 3727